

DC Magnetometry at the T_2 Limit

A. Ajoy, Y. X. Liu and P. Cappellaro

Research Laboratory of Electronics and Department of Nuclear Science & Engineering, Massachusetts Institute of Technology, Cambridge, MA

Sensing static or slowly varying magnetic fields with high sensitivity and spatial resolution is critical to many applications in fundamental physics, bioimaging and materials science. Several versatile magnetometry platforms have emerged over the past decade, such as electronic spins associated with Nitrogen Vacancy (NV) centers in diamond. However, their high sensitivity to external fields also makes them poor sensors of DC fields. Indeed, the usual method of Ramsey magnetometry leaves them prone to environmental noise, limiting the allowable interrogation time to the short dephasing time T_2^* . Here we introduce a hybridized magnetometry platform, consisting of a sensor and ancilla, that allows sensing static magnetic fields with interrogation times up to the much longer T_2 coherence time, allowing significant potential gains in field sensitivity. While more generally applicable, we demonstrate the method for an electronic NV sensor and a nuclear ancilla. It relies on frequency upconversion of transverse DC fields through the ancilla, allowing quantum lock-in detection with low-frequency noise rejection. In our experiments, we demonstrate sensitivities $\approx 6\mu\text{T}/\sqrt{\text{Hz}}$, comparable to the Ramsey method, and narrow-band signal noise filtering better than 64kHz. With technical optimization, we expect more than an one order of magnitude improvement in each of these parameters. Since our method measures transverse fields, in combination with the Ramsey detection of longitudinal fields, it ushers in a compelling technique for sensitive vector DC magnetometry at the nanoscale.

I. INTRODUCTION

Over the past two decades magnetic field sensors based on quantum systems have come of age, and fields at the few femto-Tesla level are now well within detection reach. These exquisite sensitivities often result from exploiting quantum interference, as exemplified in a wide array of technologies, including SQUIDs [1], atomic vapor cells [2, 3], and Nitrogen Vacancy (NV) center spins in diamond [4–6]. Spin qubits in the solid-state have shown their most sensitive performance when the signals of interest are oscillating at frequencies of hundreds of kHz or higher (AC fields), due to the ability to operate the sensor away from intrinsic $1/f$ noise [7] that otherwise plagues sensor performance. However, arguably many more signals of fundamental importance have low frequency or are even static (DC fields). This includes magnetic fields from biological processes, such as the firing of action potentials in single neurons [8–10], and from magnetic materials, like edge currents in topological insulators [11, 12]. This is also true for a broader class of signals that can be transduced to effective magnetic fields, such as rotations [13], pressure [14] and electric fields [15].

The conventional method for sensing DC magnetic fields is by the celebrated Ramsey technique [16], where the sensor evolves freely acquiring a phase under the field to be measured. Unfortunately, the presence of noise limits the sensor interrogation time (hence the total phase) to the *dephasing* time T_2^* . This is far shorter than the intrinsic sensor *coherence* time T_2 , often by a few orders of magnitude [17]. Indeed, the key sensitivity advantage of AC sensors derives from lengthening the interrogation times up to T_2 , by performing phase sensitive (lock-in) detection [18, 19] at the known signal frequency of interest, via a narrow bandwidth filter created by dynamical-decoupling (DD) sequences [20, 21].

Here we introduce and experimentally demonstrate an ancilla-mediated method to up-convert DC signals to AC signals, prior to quantum lock-in detection, allowing DC magnetometry at the T_2 limit. While the technique is more general, here we employ a sensor consisting of the electron spin of a single NV center in diamond and an ancillary nuclear spin qubit. Coupling to the nuclear spin up-converts the DC field to a frequency that can be tuned well beyond the environmental noise spectrum

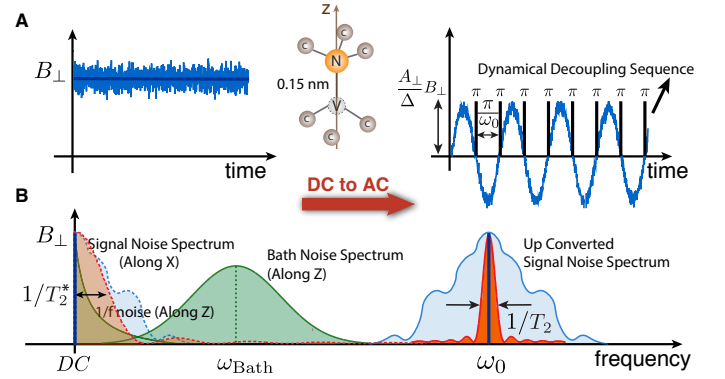


Figure 1. DC magnetometry at T_2 via ancilla assisted upconversion. (A) A magnetic field B_{\perp} with low-frequency noise is up-converted by the ancillary ^{14}N nuclear spin of an NV center (inset) to an AC signal with frequency ω_0 and amplification factor A_{\perp}/Δ . Rectification by a DD sequence (black lines indicate π pulses) performs a quantum lock-in detection at ω_0 , measuring the DC signal and rejecting noise. (B) Frequency-domain picture of the signal frequency upconversion and noise filtering. The $1/f$ and spin bath noise (green), acting on the NV sensor in the \hat{z} direction, usually limit interrogation times to T_2^* . We also consider the low-frequency noise carried by the signal (light blue) in the \hat{x} direction before (dashed lines) and after (solid lines) the up-conversion. Ancilla assisted upconversion leads to a dual band-pass filtering of both signal and sensor noise thanks to the narrow DD filter bandwidth, $\sim 1/T_2$, with a consequent gain in magnetometer sensitivity.

cut-off. The AC field is then measured by quantum lock-in-detection (rectification [22]). This frequency conversion chain (Fig. 1), from DC \rightarrow AC \rightarrow DC, enables narrowing the noise bandwidth seen by the sensor to within $1/T_2$. Our method can thus be seen as a form of quantum error correction [23], and provides significant gains in sensitivity and noise suppression – *both* of environment noise and noise carried by the signal to be sensed.

Remarkably, the same frequency upconversion can also be applied to detect low frequency (1kHz - 1MHz) AC fields, which are out of reach of conventional dynamical decoupling-based schemes. In addition, the long interrogation times make the NV sensor amenable to highly efficient readout techniques, includ-

ing charge state readout [24], providing significant sensitivity gains. The technique is particularly suited for spin ensemble sensing, by canceling inhomogeneities and providing better sensitivity per unit volume. Combined with the conventional Ramsey detection of longitudinal fields, our technique can enable sensitive, low noise, full vector nanoscale magnetometry at T_2 with a single point defect sensor.

The paper is organized as follows. Sec. II describes the ancilla-based magnetometry protocol followed in Sec. III by a sensitivity analysis. In Sec. IV we detail how our technique, based on frequency upconversion, achieves an effective low-pass filtering of signal noise and band-pass filtering of sensor noise. Sec. V evaluates practical issues affecting our technique, in particular the dynamic range. Finally in Sec. VI, we describe extensions to full vector DC magnetometry and to low-frequency AC magnetometry.

II. ANCILLA-ASSISTED DC FIELD SENSING

At the core of our method for frequency up-conversion and lock-in detection is the coherent coupling between a qubit probe and an ancillary qubit system. We assume that the quantum probe S is sensitive to the DC signal we want to detect, but the ancillary qubit I does not couple to it (or the coupling is very weak). The sensor-ancilla Hamiltonian is then:

$$H = \Delta S_z + \omega I_z + H_{\text{hyp}}, \quad \text{with}$$

$$H_{\text{hyp}} = A_{\parallel} S_z I_z + A_{\perp} (S_x I_x + S_y I_y)$$

When $\Delta - \omega \gg A_{\perp}$, the transverse part of the coupling can be neglected ($H_{\text{hyp}} \approx A_{\parallel} S_z I_z$) and the two systems can be easily decoupled, e.g., with a spin echo. However, an added transverse magnetic field, B_{\perp} that couples to the qubit sensor as $\gamma B_{\perp} S_{\perp}$, induces a mixing of the qubit/ancilla energy levels. Under the assumption $\Delta \gg A_{\perp}$, this second order process produces an effective coupling $H'_{\text{hyp}} \approx A_{\parallel} S_z I_z + \frac{\gamma B_{\perp} A_{\perp}}{\Delta} S_z I_x$. Then, in the interaction picture of the ancilla, the last term becomes time-dependent and the qubit sensor effectively sees an AC field $\propto B_{\perp} \cos(\omega_0 t)$. This simple model can be applied to many quantum sensor systems. Here we focus on the electronic spin of a single Nitrogen Vacancy (NV) center in diamond, which has been shown to have AC field sensitivities better than $1\text{nT}/\sqrt{\text{Hz}}$ [4], and nanoscale spatial resolution [25–27]. We consider using a nearby nuclear spin as an ancilla, for instance the ^{14}N nuclear intrinsic to every NV center, or a ^{13}C spin in the first few shells [28, 29]. For this system we have $\Delta = \Delta_0 - \gamma_e B_{\parallel}$ (where $\Delta_0 = 2.87$ GHz is the NV zero field splitting and $\gamma_e = 2.8$ MHz/G is the gyromagnetic ratio of electron), and the effective hyperfine interaction becomes $\frac{\gamma_e B_{\perp} A_{\perp}}{\Delta} F S_z I_x$, where F is a factor that depends on the type of ancillary spin (see Appendix A). Similarly, the frequency ω_0 of the effective AC fields will depend on the spin system considered.

The second-order mixing of the electronic and nuclear levels can be viewed as an effective frequency up-conversion [32–34] of the DC field B_{\perp} to an AC field, $\gamma_e B_{\perp} (A_{\perp} F / \Delta) \cos(\omega_0 t)$, at the resonance frequency ω_0 of the nuclear spin. In other words, the nuclear qubit is analogous to a free running oscillator at a frequency ω_0 set by nature. In the presence of the transverse magnetic field, the NV sensor couples to this oscillator, up-converting the DC field to ω_0 . This AC field can now be

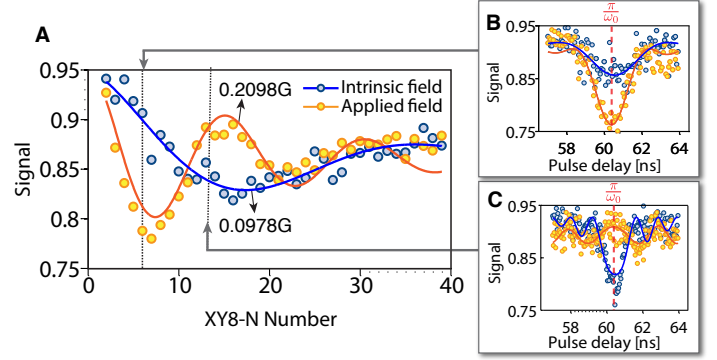


Figure 2. **Ancilla assisted DC magnetometry.** (A) Magnetometry signal at $\Delta = 141\text{MHz}$ as a function of the pulse sequence length, under intrinsic misalignment $B_i \approx 0.0978\text{G}$ (blue points) and an additional DC field $B_{\perp} \approx 0.2098\text{G}$ (orange points). The field values are obtained from the frequency of the oscillations (solid lines: fit). Each point in (A) is obtained at the optimal sensing point, $\tau = \pi/\omega_0$, from time-domain traces as shown in (B) and (C) for XY8-7 and XY8-12, respectively. We employed quantum interpolation [30, 31] to precisely sample the peaks at 35.7ps (B) and 20.8ps (C).

measured using well-known quantum lock-in techniques, based on trains of dynamical decoupling pulses, with pulse spacing set at the effective AC field period. We can for example use the CPMG/XY8 protocol [35–37] that simultaneously decouple the NV sensor from external noise, allowing interrogation up to the T_2 coherence time [38, 39].

The interferometric signal is then given by $S = \frac{1}{2}[1 + \cos(N\alpha)]$, where α is the angle between the nuclear Hamiltonians in the two NV manifolds (see Appendix A), and N the number of pulses. For small B_{\perp} fields, $\alpha \ll 1$, and to a good approximation the signal is

$$S = \frac{1}{2} \left[1 + \cos \left(\frac{\gamma_e B_{\perp} A_{\perp} N}{\omega_0 \Delta} F \right) \right]. \quad (1)$$

This signal is especially strong close to the NV center ground state level anti-crossing (GSLAC, $B_z \approx 1025\text{G}$), where $\Delta \rightarrow 0$. The signal slope is proportional to the hyperfine field A_{\perp} . For ^{14}N , this coupling is $A_{\perp} = -2.62\text{MHz}$ and $F = \frac{2\sqrt{2}(Q-A_{\parallel}/2)^2}{(Q-A_{\parallel})Q} \approx 3.1$, as determined from second order perturbation theory. Note that while the ^{14}N spin is a natural choice since it is present in every NV center, and provides the added benefit of high robustness to magnetic fields (see Appendix D), an ancillary ^{13}C spin could provide a wider dynamic range and reduce certain experimental constraints due to its strong hyperfine coupling. Indeed, for ^{13}C , $F = \frac{4(A_{\parallel} - \gamma_n B_{\parallel})}{2A_{\parallel} - \gamma_n B_{\parallel}} \approx 2$, while A_{\perp} could be substantially stronger, $A_{\perp} > 140\text{MHz}$ potentially allowing DC field sensing at large values of Δ .

While hyperfine-mediated fields have been observed before [40] to boost the Larmor [28] and Rabi [41, 42] frequencies of the ancillary nuclear spin, here instead we have employed the hyperfine for a frequency mixing action that aids quantum metrology.

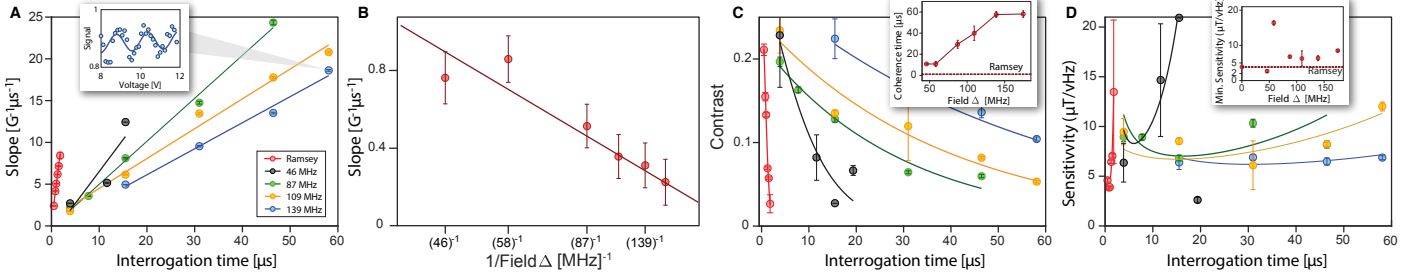


Figure 3. **Magnetometer sensitivity.** By sweeping an external DC field B_e we determine the signal sensitivity in the linear regime of the magnetometer (Fig. 5). (A) Signal slope $dS/dB_e|_{B_0}$ as a function of interrogation time for representative values of field Δ . Inset: example of magnetometry signal with applied voltage. From the signal Fourier transform we extract the signal slope (A) and decay (C). The error bars are obtained from a Lorentzian fits of the Fourier transforms. (B) Signal slope per unit time from (A) plotted as a function of Δ , showing the expected $1/\Delta$ dependence. The error bars are residuals to the inverse linear fit. (C) Decay of the signal contrast with increasing interrogation time. In the inset: coherence times extracted from the decay. The Ramsey method (dashed line) is limited by the short $T_2^* \approx 1.15 \mu\text{s}$, while our ancilla-assisted protocol is limited only by pulse error. (D) Sensitivity for the same values of Δ and interrogation time as in (A-C). Inset: best experimentally measured sensitivity. Our technique can experimentally achieve sensitivities comparable to the Ramsey method $\approx 3.86 \mu\text{T}/\sqrt{\text{Hz}}$, with additional benefits in noise suppression (Fig. 4).

III. DC MAGNETOMETER SENSITIVITY

A. Theoretical Sensitivity Bounds

The shot-noise limited sensitivity η can be found from the smallest field δB_{\perp} one could measure in the total averaging time, $M(t+t_d)$, needed to perform M measurements with interrogation time t and dead time t_d (for preparation and readout): $\delta B_{\perp} \equiv \eta/\sqrt{M(t+t_d)}$ [43]. In turns, the minimum field is estimated from its uncertainty at the most sensitive bias point B_0 [44], $\delta B_{\perp} = \frac{\Delta S}{\sqrt{M} dS/dB_{\perp}}|_{B_0}$, where ΔS is the spin projection noise $\Delta S = \sqrt{S(1-S)}$.

From the signal in Eq. (1), evaluated at the optimal time $t = N\pi/\omega_0$, we obtained the sensitivity

$$\eta = \frac{\omega_0}{A_{\perp} F} \frac{\Delta e^{(t/T_2)^p}}{C \gamma_e N} \sqrt{t+t_d} = \frac{\pi \Delta e^{(t/T_2)^p}}{C \gamma_e A_{\perp} F t} \sqrt{t+t_d}, \quad (2)$$

where we further introduced a signal decay $\propto e^{-(t/T_2)^p}$ and a factor encapsulating readout inefficiencies, C . Since the NV spin state is measured through its fluorescence, photon shot noise, finite contrast and photon collection efficiency degrade the sensitivity by this factor $1/C$ [43].

Since our method exploits DD sequences, the interrogation time t can be extended to T_2 , and the sensitivity is optimized for $t \approx T_2$. Assuming $t_d \ll t$ [45], for ^{14}N ancilla we obtain

$$\eta \approx \frac{\pi \Delta}{A_{\perp} F} \frac{1}{C \gamma_e \sqrt{T_2}} = \frac{\pi \Delta \sqrt{2} Q (Q - A_{\parallel})}{A_{\perp} 4 (Q - A_{\parallel}/2)^2} \frac{1}{C \gamma_e \sqrt{T_2}}. \quad (3)$$

We can compare this result to the Ramsey sensitivity, $\eta_R = 1/(C \gamma_e \sqrt{t})$, where the interrogation time is limited by short dephasing time $t \approx T_2^*$. Even if the ratio Δ/A_{\perp} must be kept small (to maintain the perturbative regime as well as achieve low pulse errors, see Sec. V), we can achieve an improvement over Ramsey metrology when the ratio T_2/T_2^* is large, as it is often the case (e.g., $T_2/T_2^* \sim 10^3$ in NV systems).

B. Experimental Sensitivity

To experimentally determine the sensitivity for our technique, we measure the signal slope $dS/dB_{\perp}|_{B_0}$ for a ^{14}N ancilla by sweeping an external field B_e . The field is produced by an external voltage V (Fig. 3), and it is simply proportional to V , with $B_e/V = 0.0407 \pm 0.0006 \text{ G/V}$ (obtained from the experiments described in Fig. 5). We operate in the optimal dynamic range regime of the magnetometer (see Appendix C), where the field to be measured, perpendicular to the N-V axis, is proportional to the external field $B_{\perp} \propto B_e$.

As shown in Fig. 3(A-C), at the optimal bias point the signal slope is $dS/dB_{\perp}|_{B_0} = e^{-(t/T_2)^p} \frac{\gamma_e A_{\perp} F t}{2\pi \Delta}$, i.e. it varies linearly with the interrogation time, is inversely proportional to the deviation Δ from the GSLAC, and is reduced by the signal decay. For a more accurate estimation of the slope, we measured the signal over a larger range of applied fields and used its Fourier transform to independently determine the signal decay (from the contrast, Fig. 3.C) and its dependence on B_{\perp} (from the frequency (slope), Fig. 3.A).

For comparison, we also plot the performance of conventional Ramsey magnetometry experiments under the same conditions (Fig. 3) for the measurement of the *longitudinal* magnetic field, $\cot(\vartheta)B_{\perp}$, where $\vartheta = 39.32^\circ$ is evaluated from the experiments shown in Fig. 5. In Fig. 3(B), one can clearly discern the $1/\Delta$ dependence of the signal slope showing very good agreement with theory. From Fig. 3(C), it is evident that in our technique the NV sensor is better protected against noise and much longer interrogation times are possible than in the Ramsey experiment, for in the presence of the external field, $T_2^* \approx 1.16 \mu\text{s}$ (inset of Fig. 3(C)).

We measured the signal noise $\Delta S/C \approx 17.27$ through a binning of photocounts, and estimated the magnetometer sensitivity for different values of Δ and interrogation times (Fig. 3(D)). At $\Delta = 139 \text{ MHz}$ the sensitivity of our ancilla assisted protocol $\approx 6.02 \mu\text{T}/\sqrt{\text{Hz}}$ approaches that of the Ramsey technique $\approx 3.86 \mu\text{T}/\sqrt{\text{Hz}}$ (inset of Fig. 3(D)). As explained in Appendix C, pulse errors limited the achievable interrogation times to $t \approx 60 \mu\text{s}$. The errors are higher than usual partly because of the high duty cycle (the ratio between the pulse duration and the period) of the DD sequence ($t_{\pi}/\tau \approx 0.41$ at $\tau = \pi/\omega_0 \approx 121 \text{ ns}$

and π -pulse length $t_\pi = 50\text{ns}$, and due to the residual intrinsic misalignment of about 0.3G (Appendix C). Indeed, we achieve a better coherence time, $T_2 > 350\mu\text{s}$, at lower pulse duty cycles ≈ 0.047 . Hence, by employing faster pulses, working at high nuclear harmonics (Fig. 11), and using magnetic shielding to remove intrinsic misalignment [46], we should be able to improve the pulse quality, achieve longer interrogation times, and outperform the Ramsey sensitivity. An alternative strategy (Appendix E) is to use a spin-lock pulse sequence that can achieve long coherence times ($T_{1\rho} \gg T_2^*$).

Our protocol could provide further sensitivity gains when combined with the recently developed readout via NV spin-to-charge mapping followed by charge state readout (CSR) [24]. CSR can dramatically improve the C-factor in magnetometry at the cost of an increased dead time t_d . For the Ramsey technique, t_d is a substantial fraction of the interrogation time and CSR leads to little overall gain in sensitivity. In contrast, long interrogation times, as in our method, allow to reap the benefits of CSR, as even longer dead-times are still just a fraction of the interrogation times. For example, for $t_d \approx T_2/4$, $C_{\text{CSR}} \rightarrow 10C$ for $T_2 \approx 1\text{ms}$ [47]. For the interrogation times in our system, $T_2 \approx 60\mu\text{s}$, we have $C_{\text{CSR}} \approx 2C$ [47] and the sensitivity can be improved to $\approx 3.01\mu\text{T}/\sqrt{\text{Hz}}$.

We also note that for DC magnetometry with an ensemble of NV sensors, performing the experiments at the GSLAC produces an additional boost in C-factor by ≈ 1.43 , since the photoluminescence background from off-axes families of NV centers, which do not contribute to the signal, is effectively quenched by a factor ~ 0.6 . (See Appendix F, Fig. 13 showing this effect.)

Finally, our technique leads to additional gains in sensitivity due to superior suppression of signal and sensor noise as we now explain.

IV. DUAL SUPPRESSION OF SIGNAL AND SENSOR NOISE

Since our magnetometry method exploits an ancilla-assisted frequency up-conversion of the DC field, it enables an enhanced rejection of noise and consequently interrogation times approaching T_2 . The noise rejection applies to two main sources of noise (Fig. 1) – the noise due to the local environment, always affecting the sensor (*sensor noise*), and the additional noise introduced by the magnetic field being sensed (*signal noise*). The signal noise is in the transverse (\hat{x}) direction and centered around zero or low frequency, while the sensor noise is primarily in the \hat{z} direction and centered about ω_{Bath} . As we describe in detail in Appendix B, our technique enables *low-pass* filtering of signal noise, and *band-pass* filtering of sensor noise. The filtering action is due to the combination of two factors, DD-sequence filtering with ancilla-assisted frequency upconversion. DD sequences can indeed be interpreted as creating narrow-band filters [20, 21, 48], centered around the inverse pulse period and with rejection and band-pass width inversely proportional to the number of pulses. In Ramsey magnetometry, this filter is centered around zero frequency, where the dominant $1/f$ sensor noise is maximum, and it has the widest band-pass width. In analogy with conventional lock-in-amplifiers [19], in our method the ancilla performs a frequency upconversion of the DC field to ω_0 , allowing us to lock into this frequency with a DD sequence and to effectively *narrow* the noise bandwidth seen by the sensor. In addition, since the suppression of sensor noise al-

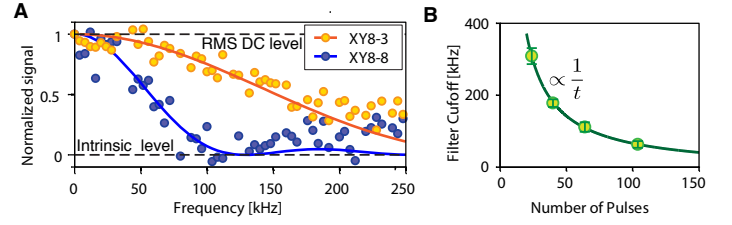


Figure 4. **Experimental low-pass filtering of signal noise.** (A) Signal depth of two XY8-N (yellow, $N = 3$, blue $N = 8$) experiments at $\Delta = 141\text{ MHz}$ as a function of the frequency of an applied magnetic field. The signal directly maps the filter function of the protocol. Three sets of data are taken concurrently: signal in the presence of an applied AC magnetic field, signal without AC magnetic field (which sets the intrinsic level), and signal in the presence of a DC magnetic field. The first set of data is normalized against these two levels. Solid lines are the theoretical low-pass filters (Eq. (10)), showing very good agreement with the experimental data. (B) Cut-off frequency of the filter, defined as the first zero crossing of the experimental signal in (A). The filter becomes narrower with increasing interrogation times (pulse number) as expected from theory (solid line), with the lowest measured point corresponding to a cutoff of 63.4kHz . In contrast, the filter for the Ramsey technique is much broader, with cutoff $1/T_2^* \approx 862.0\text{kHz}$. The error bars are obtained from fits of the theoretical low-pass filters.

lows longer interrogation times, the band-pass of the filter can be made very narrow by increasing the pulse number, thus becoming very effective in suppressing the signal-noise (which undergoes a frequency upconversion in the same way as the DC signal field).

Qualitatively similar gains in interrogation times could be achieved by exploiting an ancilla to perform quantum error correction [49–51]. Whereas these techniques could potentially go even beyond T_2 , provided feedback correction is applied faster than the error rate affecting the sensor, in our protocol the ancilla need not be initialized nor actively manipulated, greatly reducing the experimental resources required.

In Fig. 4 we experimentally demonstrate the signal noise filtering ability of our protocol, by mapping its noise filter line-shape. We reproduce the expected low-pass frequency behavior (Appendix B), where the cutoff decreases inversely with the total interrogation time t . We demonstrate a low-pass signal noise cutoff of 63.4kHz for XY8-13, in contrast to the much larger Ramsey cutoff of 869.6kHz . In principle it could be possible to reduce the signal noise with additional hardware [52], however this filter stage would inevitably increase the sensor standoff from the signal source, and thus reduce the sensitivity. Our method is then equivalent to introducing an intrinsic tunable low-pass signal filter, with just a 0.15nm additional footprint.

Signal noise rejection leads to a practical improvement in the minimum field that can be sensed. Indeed, δB_\perp decreases with the number M of measurements as $1/\sqrt{M}$, as can be evaluated by the sensor Allan deviation. However, even assuming not to be limited by drifts in the experimental setup, this shot-noise regime is bounded by the signal noise spectrum cut-off $1/\omega_n$. Hence, in the regime $T_2^* < 1/\omega_n < T_2$, a suppression in signal noise allows a gain in achievable shot-noise repetition number n_r , improving the sensitivity by a factor $\sqrt{T_2\omega_n} \leq \sqrt{T_2/T_2^*}$ over the conventional Ramsey technique.

Suppression of sensor noise is particularly beneficial for ensemble magnetometer operation, where inhomogeneities more

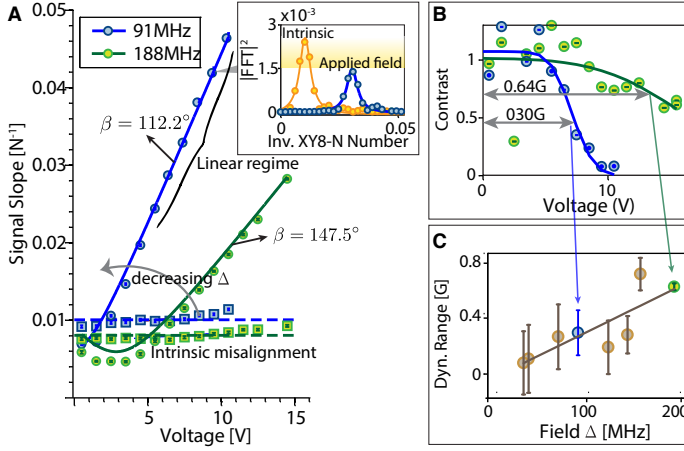


Figure 5. **Optimal operating range.** (A) From the Fourier transform of the signal as a function of XY8-N cycle number N , we extract the signal frequency dS/dN as a function of the applied transverse field B_e , for two values of the longitudinal magnetic field, Δ . Inset: representative signal Fourier transform for two magnetic fields (intrinsic misalignment B_i , and total transverse field B_\perp). The solid lines are fits following $B_\perp = \sqrt{B_i^2 + B_e^2 + 2B_i B_e \cos \beta}$ (Fig. 8). We highlight the optimal (linear) operating regime where $B_e \gg B_i$. We also extract the values of β , in-plane angle between B_e and B_i . The squares are the measured values of B_i , and dashed lines represent the mean B_i (blue and green correspond to intrinsic misalignments of 0.084G and 0.142G). Error bars are obtained from a Lorentzian fit of the Fourier transform peaks. For field values closer to the GSLAC (decreasing Δ) the signal slope $d^2S/dB_e dN$ increases, leading to increased magnetometer sensitivity (see Fig. 3). The decrease in signal contrast in the inset is an indication of finite sensor dynamic range. The contrast is plotted in (B) as a function of the applied field. We fit the data to sigmoid functions (solid lines) from which we extract the sensor dynamic range. Note that the normalization is performed with respect to the concurrently measured signal under intrinsic misalignment. (C) Dynamic range for different values of Δ , indicating that it decreases with smaller Δ . Solid line is a linear fit.

severely affect T_2^* -limited protocols. For N_v sensors per unit volume, the suppression of spin bath sensor noise via DD [17, 53] enables keeping $N_v/T_2 \approx 1$, and hence an approximately constant sensitivity per unit volume.

V. DYNAMIC RANGE AND PRACTICAL LIMITATIONS

Various experimental issues affect the ultimate performance of our method, determining the practically achievable sensitivity and the optimal operating regime. Here we consider limitations of our current experiments, as well as more general bounds and strategies to overcome them.

The dynamic range is a function of the deviation from the GLSAC, decreasing with smaller Δ . In our experiments, a chief factor affecting the dynamic range is the residual field from Earth, B_i , which sets the lower limit of the dynamic range (see Appendix C). Since this problem could be resolved simply by magnetic shielding, routinely used in precision magnetometry, here we focus instead on the upper limit to the operating range, i.e. the maximum field B_\perp that can be applied to our sensor without loss of sensitivity.

First, the presence of B_\perp causes a small tilt of the initial state

prepared after the first $\pi/2$ pulse (assumed to be ideal until now) leading to a loss in signal contrast – and hence magnetometer sensitivity – by an amount $\Delta^2/(\Delta^2 + B_\perp^2)$. This effect is negligible for $B_\perp \ll \Delta$ and it can be mitigated even if the field to be measured is large, provided it is known to some precision. For a known bias point of magnetometer operation $B_{0\perp}$, one can *compensate* the tilt with a suitable preparation pulse with flip angle $\frac{\pi}{2} - \arctan(B_{0\perp}/\Delta)$.

A second factor, affecting both dynamic range and sensitivity, is the lower quality of the pulses close to the GSLAC, which limits the efficiency of DD sequences and thus the coherence time. To obtain good pulses, we need a sufficiently large Rabi frequency Ω , such that $B_\perp \ll \Omega$. However, the Rabi frequency has also other constraints. When $\Delta \rightarrow 0$, the pulses degrade due to the breakdown of the rotating wave approximation (RWA). It is not possible to simply reduce the Rabi frequency, as the minimum allowed Rabi frequency Ω is constrained by the pulse separation time, in turn set by ω_0 , $\Omega = \omega_0$. Then, imposing $\Omega < \Delta/5$ for the RWA to hold, sets a bound on the closest approach to the GSLAC. For example, $\Delta \gtrsim 5\omega_0 \approx 20$ MHz for the ^{14}N nuclear ancilla used in our experiments. In addition, even within the RWA the pulse quality is degraded due to off-resonance effects caused by B_\perp – with a pulse error (infidelity with respect to an ideal π -pulse [54]) $\sim B_\perp^2/2\Omega^2$.

These errors are compounded upon increasing the number of pulses, especially at high duty cycles, leading to a loss of magnetometer sensitivity. However, the knowledge of the operating bias point $B_{0\perp}$ would allow pulses to be suitably calibrated and optimized, even going beyond the RWA [55–57]. Furthermore, the use of higher order pulse sequences, widely developed in the NMR community [58, 59], can suppress these errors to a large extent.

The presence of a finite dynamic range is evident in the decay of the curves in Fig. 2, the pulse error compensation of XY8 sequences being slightly imperfect at high pulse number. We perform a detailed experimental characterization (Fig. 5) of the sensor dynamic range by determining the loss in signal contrast upon sweeping the external magnetic field (voltage), for increasing XY8 cycle number, and for different values of Δ . Fig. 5(B) shows a representative example of this behavior – at high applied voltages, there is a sharp loss of contrast beyond the sensor dynamic range. By performing a fit to a sigmoidal function $\sim \frac{\exp(-B_e - B_t)}{[1 + \exp(-B_e - B_t)]}$, we extract the turning point B_t that serves as a good measure of the sensor dynamic range. From Fig. 5(C) it is evident that the dynamic range decreases as one approaches the GSLAC.

VI. APPLICATIONS & OUTLOOK

A. Nanoscale vector magnetometry

Combining our technique with conventional Ramsey DC magnetometry can be the basis for a protocol for *vector* magnetometry of DC fields [60, 61] with a *single* NV sensor, with nanometer spatial resolution. Acquiring vectorial information about magnetic and electric fields would be of great benefit in many practical applications, from bioimaging (e.g. for neuronal magnetic fields [9]) to materials science. In the vector magnetometry protocol, Ramsey magnetometry measures the longitudinal (B_{\parallel}) component of the field, while our ancilla-assisted

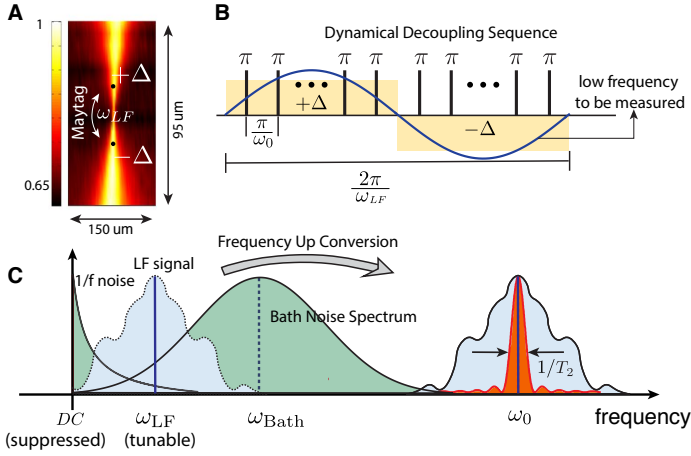


Figure 6. **Maytagging for low frequency AC magnetometry.** Schematic illustration of the proposed method for sensing low-frequency AC fields. (A) NV photoluminescence in an XZ magnet scan close to the GSLAC (see Fig. 13). (B) Pulse sequence for low-frequency magnetometry, where we alternate (maytag) the field between two values of Δ symmetric with respect to the GLSAC, at a rate ω_{LF} (as low as $1/T_2$). (C) Frequency domain representation, wherein the signal at ω_{LF} is up-converted to ω_0 and detected via dynamical decoupling.

technique detects its transverse component (B_{\perp}). For instance from the experiments shown in Fig. 3, we determine the polar angle of the field to be $\vartheta = 39.32^\circ$ ($\tan(\vartheta) = B_{\perp}/B_{\parallel}$). In order to further determine the direction of B_{\perp} in the transverse plane, one can apply a bias transverse field in a known direction (say \hat{x}). By measuring again the total transverse field with the ancilla-assisted technique, one can extract the direction of the unknown B_{\perp} (its azimuthal angle φ with respect to \hat{x}). Note that this is equivalent to experiments described in Fig. 5.

B. Low Frequency AC Magnetometry

Variants of our technique can also be applied to sense low frequency fields that are outside of range of usual DD sensing. This would be an invaluable tool for measuring several ubiquitous fields of experimental significance that have low frequency (30kHz - 1MHz). For instance, this a common occurrence for impulse response fields from magnetic materials [62], where the repetition rate is often material-limited to $\omega_{LF} < 1\text{MHz}$. Unfortunately the conventional echo-based AC field sensing techniques require the pulsing frequency to be exactly matched with the frequency one wants to sense, which is not possible when $\omega_{LF} \ll 1/T_2^*$ due to sensor dephasing. Hence the low frequency regime is a “blind-spot” for conventional magnetometry [63].

Due to the narrowband low pass filtering behavior of the sensor, we cannot directly use our method to measure low frequency AC field. However, an extension of the method, inspired by field reversals employed in MEMS technology [64], can detect slowly varying fields. We alternate (maytag) the applied longitudinal magnetic field between two values that reverse the sign of Δ (Fig. 6), with the maytagging frequency equal to the frequency of interest, ω_{LF} . In the experiments, this can be achieved for instance by the application of a fast switching control voltage inducing a B_z field, in addition to a fixed bias field at the GSLAC condition, $\Delta = 0$. Maytagging leads to *amplitude* mod-

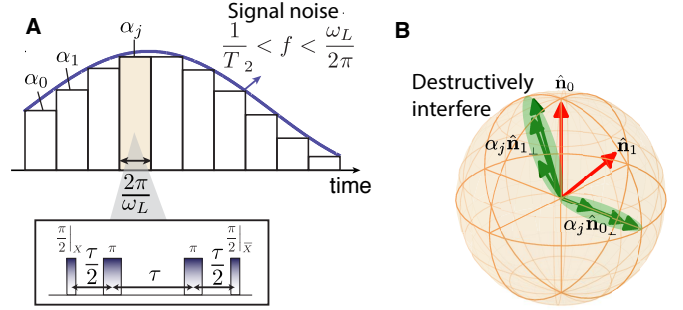


Figure 7. **Low frequency noise rejection in ancilla-assisted magnetometry.** Schematic derivation of the low-pass signal noise filter inherent to our protocol. (A) Consider a low frequency magnetic noise tone of frequency $f \ll \omega_0$. Each rectangular block corresponds to a CPMG pulse sequence (inset) of total time $2\tau = 2\pi/\omega_0$. To a good approximation the signal results from the combined effect of the tilt angle $\alpha_j = B_{\perp}^{(j)} A_{\perp} F/\Delta$, discretized over the L CPMG blocks. (B) Geometric visualization of filtering action. Here \hat{n}_0 and \hat{n}_1 (red arrows) are the axes of nuclear rotation. For a *static* DC field, the effective vectors are perpendicular to the original axes and anti-parallel leading to a strong signal through constructive interference. However in the presence of low-frequency signal noise, these open up a fan of vectors (green arrows), for instance $\alpha_j \hat{n}_1^{(j)}$, over which the effective propagator needs to be evaluated. This leads to destructive interference, and consequently signal noise suppression that increases with number of pulses.

ulation of the field to be sensed, $B_{\perp}(t)A_{\perp}/[\Delta \cos(\omega_{LF}t)]$, and only frequencies in $B_{\perp}(t)$ that match the maytagging frequency contribute to the signal. All other components, including the DC component, are filtered out in the same manner as the filtering of signal noise in Fig. 4 (see Appendix B for a detailed derivation).

Crucially, this sensing frequency is now under experimental control, and can be as low as $1/T_2$ with no loss in sensitivity. Importantly, this enables moving away from the zero frequency point where the $1/f$ noise has a significant contribution. In summary therefore, a tunable frequency up-conversion from a low ω_{LF} to a high-frequency ω_0 using our method, allows one to decouple the pulsing frequency from the sensing frequency in conventional AC magnetometry.

VII. CONCLUSIONS

We have demonstrated a new modality for high sensitivity magnetometry through a frequency upconversion mediated by an ancillary nuclear spin, combined with quantum lock-in detection, allowing low noise DC magnetometry at the T_2 limit. In contrast, conventional DC magnetometry is limited by the much shorter dephasing time T_2^* . The technique leads to an enhanced suppression of noise, both of the external noise on the sensor as well as the noise associated with the signal being sensed. For sensors based on NV centers in diamond, this could enable substantial gains in DC sensitivity over the conventional Ramsey method, especially when coupled with spin-to-charge conversion and readout. In conjunction with Ramsey spectroscopy, our technique enables full vector DC magnetometry at the nanoscale. Similar upconversion ideas can be applied to the sense low frequency AC fields. We anticipate applications of our sensing technique in many areas of biology and condensed matter physics, and for the transduced sensing

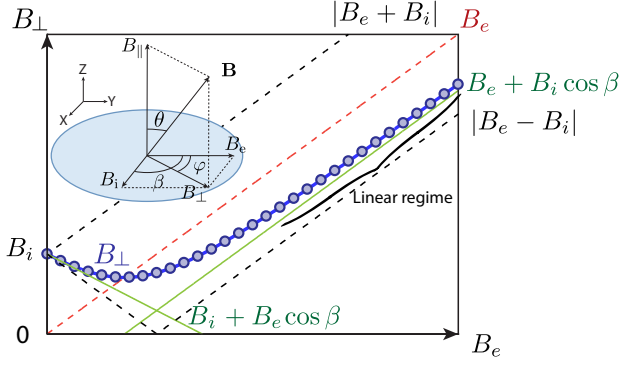


Figure 8. **Geometric interpretation of optimal magnetometer operating regime.** The effective field $|B_{\perp}|$ is the vector sum (inset) of the external field to be measured B_e and the intrinsic misalignment B_i , separated by the angle β (here $\beta = 3\pi/4$). Green lines denote asymptotes in the extremal regimes $B_e \gg B_i$ and $B_e \ll B_i$, while black dashed lines are the extreme values of $|B_{\perp}|$, for $\beta = 0, \pi$. In the regime $B_e \gg B_i$, the total field grows linearly with B_e , and there is no loss of sensitivity due to intrinsic misalignment. This is the optimal operating regime for the NV sensor (see also Fig. 10). The experiments of Fig. 5, where the signal slope measures B_{\perp} , clearly reproduce the behavior depicted here.

of rotations, pressure and electric fields.

Acknowledgments – We gratefully acknowledge discussions with S. Bhawe, R. Walsworth, F. Jelezko, J. Barry, D. Glenn, L. Marseglia, U. Bissbort, J.C. Jaskula and K. Saha. This work was supported in part by the NSF CUA and the U.S. Army Research Office.

A. SECOND ORDER PROCESS PRODUCING MAGNETOMETRY SIGNAL

We consider more in detail the second order process that leads to the DC magnetometry signal close to the GSLAC. The effective Hamiltonian of the coupled NV- ^{14}N ancilla system is, $H = H_0 + V$ where,

$$H_0 = \Delta_0 S_z^2 + B_z(\gamma_e S_z + \gamma_n I_z) + Q_0 I_z^2 + A_{\parallel} S_z I_z, \quad (4)$$

is the dominant interaction, and

$$V = \gamma_e B_{\perp} S_x + \frac{A_{\perp}}{2}(S_+ I_- + S_- I_+), \quad (5)$$

is the perturbation. We define $\Delta \equiv \Delta_0 - \gamma_e B_z$ and $Q \equiv Q_0 + \gamma_n B_z$ (note that γ_e is positive, Q_0 and γ_n are negative). Both NV electronic spin and ^{14}N nuclear spin are spin-1 systems, but for simplicity we only consider the $m_s = |0\rangle, |-1\rangle$ manifold and $m_N = |+1\rangle, |0\rangle$ manifold, where the evolution occurs. Through a Schrieffer-Wolff transformation [65, 66] the perturbed Hamiltonian $H_0 + V$ is transformed to a block-diagonal form

$$H_{\text{eff}} = |0\rangle\langle 0| H_{|0\rangle} + |-1\rangle\langle -1| H_{|-1\rangle}, \quad (6)$$

where $H_{|0\rangle} = \mathbf{n}_0 \cdot \hat{\sigma}$, $H_{|-1\rangle} = \mathbf{n}_{-1} \cdot \hat{\sigma}$, with

$$\mathbf{n}_0 = \left[\frac{1}{2\sqrt{2}} A_{\perp} \gamma_e B_{\perp} \left(\frac{1}{A_{\parallel} - \Delta} + \frac{1}{A_{\parallel} - Q - \Delta} \right), 0, \frac{1}{2} \left(Q + \frac{A_{\perp}^2}{Q - A_{\parallel} + \Delta} \right) \right], \quad (7)$$

$$\mathbf{n}_{-1} = \left[\frac{1}{2\sqrt{2}} A_{\perp} \gamma_e B_{\perp} \left(\frac{1}{\Delta} + \frac{1}{Q - A_{\parallel} + \Delta} \right), 0, \frac{1}{2} \left(Q - A_{\parallel} + \frac{A_{\perp}^2}{Q - A_{\parallel} + \Delta} \right) \right]. \quad (8)$$

Since the norms of \mathbf{n}_0 and \mathbf{n}_{-1} are close, to a good approximation the ancilla spin resonance frequency is $\omega_0 = \frac{1}{2} \left(Q + \frac{A_{\perp}^2}{Q - A_{\parallel} + \Delta} \right) + \frac{1}{2} \left(Q - A_{\parallel} + \frac{A_{\perp}^2}{Q - A_{\parallel} + \Delta} \right) = Q - \frac{A_{\parallel}}{2} + \frac{A_{\perp}^2}{Q - A_{\parallel} + \Delta}$. The angle between \mathbf{n}_0 and \mathbf{n}_{-1} is $\alpha \approx \sin \alpha = \frac{\mathbf{n}_0 \times \mathbf{n}_{-1}}{|\mathbf{n}_0| |\mathbf{n}_{-1}|} \approx \frac{\gamma_e B_{\perp} A_{\perp}}{\Delta \omega_0} F$, where we defined $F \equiv \frac{2\sqrt{2}(Q - A_{\parallel}/2)^2}{(Q - A_{\parallel})Q}$.

In a CPMG sequence, the delay between pulses τ is typically swept (Fig. 2), and when the delay matches the condition $\tau = \pi/\omega_0$, the signal is interferometrically obtained as an effective overlap of two propagators conditioned on the NV state, $\mathcal{U}_{|0\rangle} = \exp(-i\alpha\sigma \cdot \hat{\mathbf{n}}_{1\perp})$ and $\mathcal{U}_{|-1\rangle} = \exp(i\alpha\sigma \cdot \hat{\mathbf{n}}_{-1\perp})$, and is of the form $S = \frac{1}{2} \left[1 + \frac{1}{2} \text{Tr} \left\{ \text{Re} \left(\mathcal{U}_{|0\rangle}^{\dagger} \mathcal{U}_{|-1\rangle} \right) \right\} \right]$. With increasing interrogation times, effectively achieved through the application of larger number N of π -pulses, there is a linear phase accumulation in the interferometric detection [30], $\text{Tr} \left\{ \mathcal{U}_{|0\rangle}^{N/2} \mathcal{U}_{|-1\rangle}^{N/2\dagger} \right\} = 2 \cos^2(N\alpha/2) - 2(\hat{\mathbf{n}}_{0\perp} \cdot \hat{\mathbf{n}}_{-1\perp}) \sin^2(N\alpha/2)$. The last term is responsible for the growing signal strength with pulse number, giving $S = 1 - \sin^2(N\alpha/2) \cos^2(\alpha/2) \approx \frac{1}{2} (1 + \cos(N\alpha)) = \frac{1}{2} (1 + \cos(N \frac{\gamma_e B_{\perp} A_{\perp}}{\Delta \omega_0} \frac{2\sqrt{2}(Q - A_{\parallel}/2)^2}{(Q - A_{\parallel})Q}))$ (see Fig. 2).

A similar derivation can be made for the NV- ^{13}C coupled system. We obtain $F = \frac{4(A_{\parallel} - \gamma_n B_{\parallel})}{2A_{\parallel} - \gamma_n B_{\parallel}} \approx 2$ and we consider $\omega_0 = \gamma_n B_{\parallel}$ for maximum signal contrast in the sensitivity calculation.

B. INTERFERENCE PICTURE OF LOW PASS SIGNAL NOISE FILTERING

We now consider the ability of our ancilla assisted DC magnetometry protocol to effectively act as a low pass filter for the noise carried by the field to be sensed (signal noise). This signal noise could be for instance, amplitude modulations in the field originating at the signal source. Here we derive the effective filter function of the signal noise employing a first order Magnus expansion [67].

To derive the noise filter function, we decompose the signal noise into low frequency AC tones of frequency f and obtain the signal as a function of f . Considering L cycles of the CPMG experiment and assuming that one works in the regime, $1/T_2 < f < \omega_0/2\pi$, to a very good approximation perturbation theory can be applied piece-wise (Fig. 7(A)) over each of the L blocks, giving rise to the effective angles $\alpha_j = \gamma_e B_{\perp}^{(j)} A_{\perp} F / (\Delta \omega_0)$ proportional to the field value $B_{\perp}^{(j)}$ at every mean interval. Note that while considering a ^{14}N ancilla, $\omega_0/2\pi \approx 3.87\text{MHz}$, and $1/T_2 \approx 1\text{kHz}$, hence our analysis is valid for a wide range of signal noise frequencies.

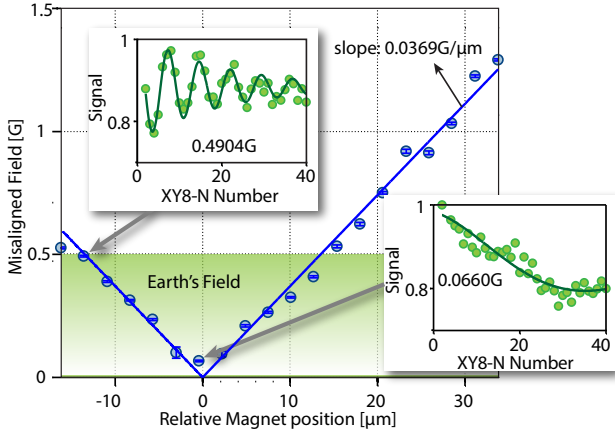


Figure 9. **Control of intrinsic misalignment.** Transverse field introduced by translating the magnet along the X direction at $\Delta = 153\text{MHz}$. The field variation with magnet displacement is very close to linear (solid lines are a fit with slope $0.0369\text{ G}/\mu\text{m}$), allowing one to adjust or minimize the field misalignment. The misaligned field here is estimated by XY8 experiments sweeping the cycle number (insets), with error bars obtained from a Lorentzian fit of their Fourier transforms. The shaded region represents misalignment at the $< 0.5\text{G}$ level, comparable to the Earth field.

$$S \propto \text{Tr} \left\{ \mathcal{U}_{|0\rangle}^{\text{eff}\dagger} \mathcal{U}_{|-1\rangle}^{\text{eff}} \right\} = \cos(L\sqrt{\mathcal{A}^2 + \mathcal{B}^2}) \cos(L\bar{\alpha}) - \frac{\mathcal{B}}{\sqrt{\mathcal{A}^2 + \mathcal{B}^2}} \sin(L\bar{\alpha}) \sin(L\sqrt{\mathcal{A}^2 + \mathcal{B}^2}), \quad (9)$$

where $\bar{\alpha} = \frac{1}{L} \sum \alpha_j$ and $\mathcal{A} = -\frac{1}{L} \sum \alpha_j \sin \alpha_j$; $\mathcal{B} = \frac{1}{L} \sum \alpha_j \cos \alpha_j$. For weak noise, $\|\alpha_j\| \ll 1$, to first order we have $\mathcal{A} \approx 0$; $\mathcal{B} \approx \bar{\alpha}$ and to a good approximation $S \propto \text{Tr} \left\{ \mathcal{U}_{|0\rangle}^{\text{eff}\dagger} \mathcal{U}_{|-1\rangle}^{\text{eff}} \right\} \approx \cos 2L\bar{\alpha}$. Let us consider the concrete case of a single noise tone of frequency $f = 1/(\tau L_p)$, where L_p refers to the effective CPMG cycle number required to complete one period. Then, assuming $\alpha_j = \alpha \cos \left(\frac{\pi j}{L_p} + \varphi \right)$ and small α , we obtain

$$S \propto \cos \left\{ 2\alpha \cos \left(\frac{\pi(L+1)}{2L_p} + \varphi \right) \frac{\sin \left(\frac{\pi L}{2L_p} \right)}{\sin \left(\frac{\pi}{2L_p} \right)} \right\} \quad (10)$$

Here φ refers to the phase of the noise tone with respect to the start of the pulse sequence, and to derive the effective filter one has to perform an average over φ . Importantly, the filter characteristics is set by the second term in the argument of Eq. (10) which has a form analogous to a Bragg grating [21, 68], with filter width $f = 1/(2L_p\tau)$ set by its first zero, and filter suppression increasing linearly with L , giving a low-pass bandwidth of $1/T_2$ in the extreme case.

The action of the frequency tone has a very clear geometric description in the space of unitary vectors (see Fig. 7(B)): for the propagator $\mathcal{U}_{|-1\rangle}$ we have an effective shortening of the corresponding vector, while for $\mathcal{U}_{|0\rangle}$ we have a fan of vectors over which the effective propagator has to be evaluated. In essence, for purely DC fields the signal terms in each cycle are all fixed strength, leading to a constructive rotation by the same amount. On the other hand, AC fields lead to scrambling of the rotations

Now, one can evaluate the *effective* propagators $\mathcal{U}_{|0,-1\rangle}^{\text{eff}}$ over the entire sequence by taking the product, $\mathcal{U}_{|0,-1\rangle}^{\text{eff}} = \prod_j \mathcal{U}_{|0,-1\rangle}^{(j)}$. In order to illustrate the key physics of low-pass signal noise filtering, for simplicity, we consider the case of a spin-1/2 ancilla, and neglect the contributions of terms $\propto I_x$ in the perturbation theory. While this makes no difference to the noise filters obtained, it allows a dramatic simplification of the analytic formalism. For instance, since the axis $\hat{\mathbf{n}}_{0\perp}$ is the same for all of the cycles, the propagator $\mathcal{U}_{|0\rangle}^{\text{eff}}$ is particularly simple to calculate: $\mathcal{U}_{|0\rangle}^{\text{eff}} = \exp(-i \sum_j \alpha_j \sigma \cdot \hat{\mathbf{n}}_{0\perp})$. It is evident that for high frequency signal noise components, for which $\sum_j \alpha_j \approx 0$, the signal is suppressed as $\mathcal{U}_{|0\rangle}^{\text{eff}} \approx \mathbb{1}$. That is, there is *destructive* interference between different CPMG cycles and the noise component is effectively filtered out. It is such destructive interference, which increases proportionally to the number L of cycles, that determines the signal noise filter.

By similarly evaluating $\mathcal{U}_{|-1\rangle}^{\text{eff}}$ with a zeroth order Magnus expansion, we obtain the signal,

and effectively destructive interference, with the filter suppression increasing with the effective time of the sequence. Hence, our ancilla-assisted protocol leads effectively to a low pass filter for signal noise and a band-pass filter for sensor noise, both with bandwidth $1/T_2$.

In comparison, the Ramsey method achieves poor filtering [21, 69], the filter being of the form $F = [\sin(\pi\omega T_2^*)/\omega]^2$, having bandwidth $1/T_2^*$, which could be two orders of magnitude larger than achievable in our experiment (Fig. 4). In effect then, the noise on the sensor due to spins in the NV environment set a bound on the amount of filtering one can achieve for the noise carried by the field being sensed.

C. EFFECT OF INTRINSIC MISALIGNMENT ON SENSITIVITY AND OPERATING RANGE

We refer to intrinsic misalignment B_i as the residual field away from the ground state anti-crossing, due chiefly to the magnetic field of the Earth. In principle this can be eliminated to about a part per million through magnetic shielding [46], a conventional choice for ultra-sensitive magnetometers. However, in our experiments without any shielding, intrinsic misalignment imposes limitations of sensor operating range, effectively setting an optimal bias point for sensor operation as we shall describe below.

More precisely, the field to be measured \vec{B}_e , and \vec{B}_i are both perpendicular to the N-V axis but are separated by an angle β ; hence the field one measures is the vector sum $\vec{B}_\perp = \vec{B}_e + \vec{B}_i$,

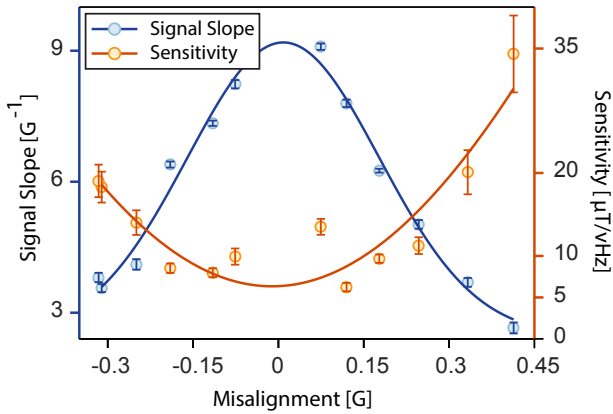


Figure 10. **Effect of intrinsic misalignment on sensitivity.** NV magnetometer DC sensitivity (orange) and the signal slope $dS/dB_e|_{B_0}$ excluding signal decay (blue), measured for different values of intrinsic misalignment B_i . Experiments correspond to XY8-48 (interrogation time $46.47\mu\text{s}$) at $\Delta = 174.5\text{MHz}$. Misalignment is controllably added following Fig. 9. Error bars are calculated from Lorentzian fits of the Fourier transforms of the obtained magnetometer fringes. The solid lines are gaussian fits to guide the eye. As is evident, increasing intrinsic misalignment has a deleterious effect on sensitivity, and for optimal sensor performance one would operate the NV sensor in the linear regime $B_e \gg B_i$, or employ magnetic field shielding.

with $B_{\perp} = \sqrt{B_e^2 + B_i^2 + 2B_e B_i \cos \beta}$. An increasing B_e , in general, leads to a nonlinear response of the sensor (see Fig. 8). Indeed in the regime where $B_e \ll B_i$, the effective field is approximately given by $B_{\perp} \approx B_i + B_e \cos \beta$, leading to an effective loss of sensitivity by $\cos \beta$. As $\beta \rightarrow \pi/2$, the field sensitivity vanishes to first order, as increasing B_e goes into changing the direction of B_{\perp} rather than its amplitude. In the opposite regime when $B_e \gg B_i$, which we shall refer to as the *linear regime*, we effectively have $B_{\perp} \approx B_i \cos \beta + B_e$, for which there is no loss of sensitivity. More generally, we have that the rate of change, $dB_{\perp}/dB_e = \left[\frac{B_e + B_i \cos \beta}{B_{\perp}} \right] = \cos \varphi$, where φ is the angle of the resultant vector \vec{B}_{\perp} to \vec{B}_e (Fig. 8). This allows us to concretely quantify the onset of the linear regime as being where $\varphi \lesssim \pi/8$. The presence of the linear regime is evident in the experiments of Fig. 5(B), where the signal slope upon sweeping XY8-N cycle number immediately reflects B_{\perp} . In the figure, the solid lines are fits to the theoretical result above. Note that the values β differ for different Δ values due to our magnet alignment procedure (Appendix F).

In order to experimentally study the effect of intrinsic misalignment on sensitivity, we increase B_i in a controllable fashion following Fig. 9, and perform ancilla assisted DC magnetometry at every point. The results in Fig. 10 indicate that intrinsic misalignment leads to a loss in sensitivity, and severely affects sensor performance; thus in experiments to characterize and operate the NV magnetometer (for instance Fig. 3), we always work in the linear regime – by suitable alignment of the magnetic field we can reliably reduce $B_i < 0.3\text{G}$ (Appendix F).

D. ROBUSTNESS OF ^{14}N ANCILLA TO MAGNETIC FIELD DRIFT

Not only has the ^{14}N ancilla the inherent advantage of being a part of every NV center sensor, it also offers significant additional benefits from a noise rejection perspective. First, note that since the resonance frequency $\omega_0 = Q - \frac{A_{\parallel}}{2} + \frac{A_{\perp}^2}{Q - A_{\parallel} + \Delta}$ is dominated by the large quadrupolar interaction $Q_0 = -4.95\text{MHz}$ ($Q = Q_0 + \gamma_n B_z$), the upconversion frequency is much higher than for the intrinsic Zeeman field $\gamma_n B_z \approx 300\text{kHz}$ alone. This not only helps in suppressing sensor noise, but it also allows a significant suppression of the signal noise. More remarkably, the frequency ω_0 is to first order immune to magnetic field drift, since its relative change is extremely small, $\delta\omega_0/\omega_0 \approx \gamma_n \delta B_z / (Q - A_{\parallel}/2) = (7.75 \times 10^{-5}) \cdot \delta B_z$. This ensures that the frequency employed for quantum lock-in detection, (dynamical decoupling sequences with quantum interpolation [31]), is robust against field drift. Even if magnetic field drifts change Δ , this only induces an effective amplitude modulation of the up-converted field (which is $\propto A_{\perp}/\Delta$), which is exactly the signal noise that can be suppressed to better than $1/T_2$ by our protocol (Sec. IV). Hence the ^{14}N ancilla affords an inherent robustness to magnetic field drift, and provides an enabling experimental advantage.

In order to demonstrate this experimentally (Fig. 11), we performed experiments at $\Delta = -893\text{MHz}$ (1344G), where the ^{14}N frequency, $\omega_0 \approx 3.87\text{MHz}$, is very close to what obtained close to the GSLAC (see Fig. 2). Close to the GSLAC we detect only one set of echo modulation [70, 71] (at ω_2 in Fig. 11) since the ^{14}N polarized by optically mediated polarization exchange with the NV electronic spin [72]. However at large Δ , as in Fig. 11, the ^{14}N is not polarized, and the two sets of modulations at the odd harmonics of the frequencies $\omega_{1,2} = Q \pm A_{\parallel}/2 \pm \gamma_n B_z \mp A_{\perp}^2/4\Delta$ are clearly discernible, which allows more choices for the up-conversion frequency ω_0 . The presence of the higher harmonics also points to the ability to perform experiments in a suitable pulse duty cycle regime where the pulse error can be minimized.

E. SPIN-LOCK DC MAGNETOMETRY

We now consider an alternative strategy for ancilla-assisted DC magnetometry via spin locking [73, 74] (Fig. 12(A)). The NV center is spin locked at a Rabi frequency Ω , and at the Hartmann-Hahn matching condition [75, 76] $\Omega = \omega_0$, there is once again a second-order hyperfine mixing $\propto B_{\perp} A_{\perp}/\Delta$ that causes a flow of polarization away from the NV center, which can be detected. In essence, this method is a rotating frame analogue of the dynamical decoupling protocol we employed in the main paper. The signal has exactly the same form of Sec. II, $S = \frac{1}{2}[1 + \cos(\alpha t)]$, where t is the spin-lock time, and $\alpha = \gamma_e B_{\perp} A_{\perp} F/\Delta$. This method also benefits from the same ancilla-assisted frequency upconversion that enabled signal and sensor noise suppression. Overall, spin-lock DC magnetometry might offer some additional advantages: (i) the Hartmann-Hahn matching requires careful adjustment of the drive amplitude, but does not require quantum interpolation; (ii) since decoupling is applied continuously, a larger amount of the sensor noise spectrum can be effectively suppressed, quantified by the coherence time $T_{1\rho}$ that is usually greater than echo-based T_2 . In prac-

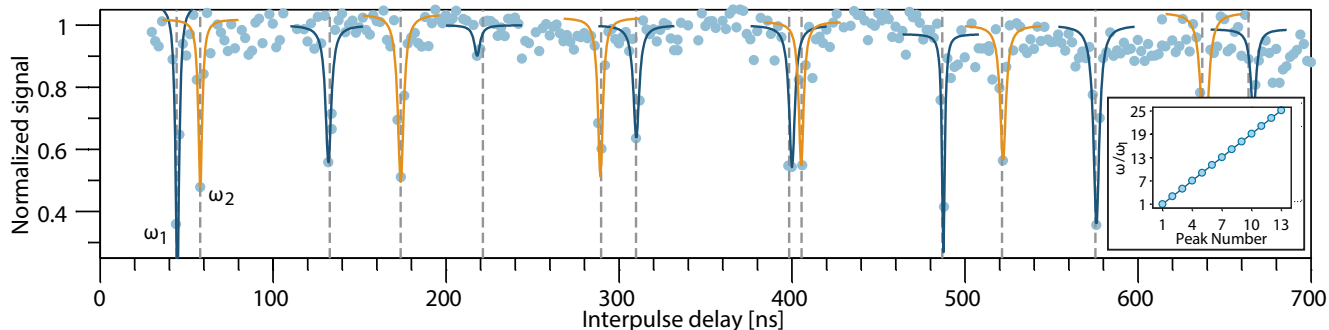


Figure 11. **Signal harmonics in ^{14}N assisted magnetometry.** DC magnetometry signal at 1344G (893 MHz) for long inter-pulse times showing families of harmonics from the ^{14}N ancilla, occurring at $\omega_{1,2} = Q \pm A_{\parallel}/2 \pm \gamma_n B_z \mp A_{\perp}^2/4\Delta$. The two sets of harmonics, indicated by the orange and blue peaks, respectively, correspond to nuclear spin transitions in the $m_I = \pm 1$ manifolds. Gray lines indicate the theoretically expected values of the harmonics. In the inset: frequency of the blue peaks as a function of ω_1 , showing that we measure odd ^{14}N harmonics as expected. To minimize pulse errors, one can select a harmonic with a suitable duty cycle.

tice however, amplifier noise sets the ultimate coherence time achievable [77]. In Fig. 12(B) we present example spin lock DC magnetometry data at $\Delta = 165\text{MHz}$, indicating that an interrogation time of over $350\mu\text{s}$ is achievable. A detailed analysis of magnetometer sensitivity using spin-lock techniques will be presented elsewhere. The good performance of spin-lock DC magnetometry indicates that the pulsed scheme interrogation time (and hence sensitivities) is primarily limited by pulse error, and can be mitigated through higher order pulse compensation [59].

F. MAGNETIC FIELD ALIGNMENT AT THE GSLAC

To align the magnetic field [31] near the GSLAC (1025G), we exploit the fact that the NV center photoluminescence (PL) gets quenched with increasing misalignment due to level mixing in the excited state [78, 79] (Fig. 13(B)). We employ a permanent magnet in our experiments, and translating the magnet in the X and Y directions to find the position of maximum photo-

luminescence leads to an alignment to better than 1° [31]. An experimental 2D XZ map of NV photoluminescence illustrates this more clearly, (Fig. 13(C)), the narrow neck corresponding to the GSLAC. We note that this sharp feature in the NV photoluminescence as a function of misalignment at the GSLAC could be used as the basis for an all-optical magnetometer, as it was recently demonstrated [80].

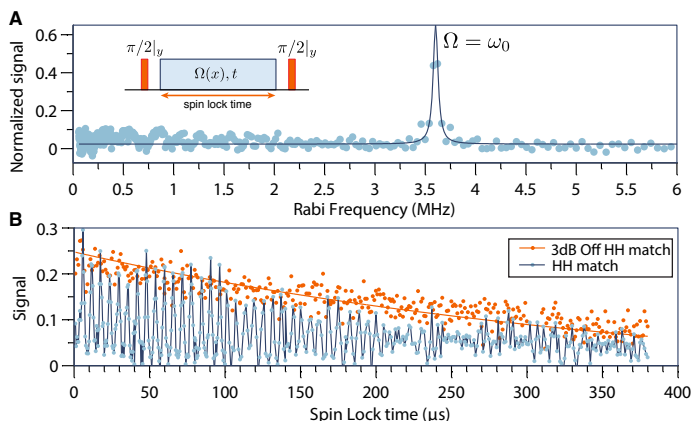


Figure 12. **Spin lock ancilla assisted DC magnetometry** (A) Spin lock measurements performed at 717G, with lock length fixed at $10\mu\text{s}$, and sweeping Rabi frequency Ω . We obtain a magnetometry signal at the Hartmann-Hahn match $\Omega = \omega_0$. Inset shows the pulse sequence. (B) Sweeping spin lock time at $\Delta = 165\text{MHz}$ at the Hartmann-Hahn match (blue) and 3dB away (orange). The oscillations constitute the DC magnetometry signal, exactly analogous to Fig. 5. Crucially we are able to extend the sensor interrogation time $> 350\mu\text{s}$.

The NV center resonance frequency Δ changes linearly as a function of the magnet height, and can be made to approach zero close to the GSLAC (Fig. 13(D)). To further optimize the alignment, down to the intrinsic contribution given by the Earth's field ($< 0.3\text{G}$), we employ a gradient ascent algorithm to find the highest photoluminescence in the GSLAC region (shaded), and extrapolate linearly from this region, exploiting the linear behavior of the NV resonance frequency with magnet distance. The small PL variance in the GSLAC neck ensures that the alignment procedure is reproducible and accurate (Fig. 13(E)). We note that when the field is aligned with the NV axis, the ^{14}N nuclear spin is completely polarized via a hyperfine-mediated optical process [72], further increasing the signal contrast obtained in the magnetometry experiments.

The amount of misalignment can be accurately measured through an XY8 experiment, sweeping the number of pulses and extracting the frequency f_0 of the resulting oscillations (Fig. 9), following $B_{\perp} = \tan(f_0/2) \frac{\Delta\omega_0}{\gamma_e A_{\perp} F}$. We are able to reproducibly align the field to better than 0.1G , this $\sim 0.01\%$ residual error largely being set by the magnetic field of the Earth. Translating the magnet along the X axis also allows the controllable addition of misalignment in an approximately linear manner, and enables quantifying the effect of the residual Earth's field on the sensor dynamic range (Appendix C).

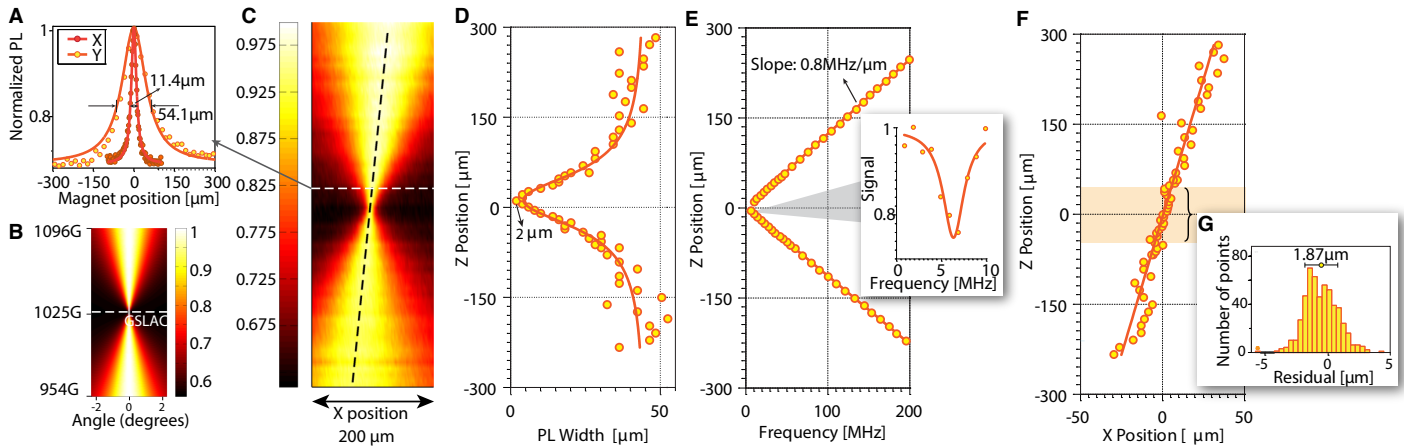


Figure 13. **Alignment of magnetic field close to GSLAC.** (A) NV center photoluminescence (PL) intensity as a function of magnet position along X and Y, showing a high sensitivity to misalignment close to the GSLAC ($B_z = 1025\text{G}$). (B) Simulations of NV PL as a function of misalignment angle and magnetic field. (C) Experimental NV PL in an XZ magnet scan [31]. The narrow neck is the anti-crossing point (GSLAC). The dashed black line indicates where the PL is maximized (best alignment with the NV axis). (D) For each Z position, we extract from a Lorentzian fit the width of the PL curves (see panel A) as a function of the magnet position X. The solid line is a Lorentzian fit to these widths. At the GSLAC, the PL width is under $5\mu\text{m}$. (E) NV electronic resonance frequency Δ as a function of the Z magnet position. The frequency varies linearly with Z (the solid line is a linear fit). We can reduce the NV resonance frequency down to $\Delta \approx 6\text{MHz}$. Inset: shows this through pulsed ODMR. (F) Optimization of field alignment via a gradient ascent algorithm. At each Z position, the circles are alignment positions for magnet X position. Near the GSLAC neck the PL has a larger gradient so the algorithm is more robust to noise and we can align the field better. The solid line is a linear fit only using points near the GSLAC neck (shaded). (G) Inset represents a histogram of the residuals to the fit in the shaded region over 36 such datasets, showing that the average error of magnet alignment close to the GSLAC is reproducibly under $1\mu\text{m}$ (about 0.1 Gauss).

-
- [1] J. Clarke and A. I. Braginski, *The SQUID handbook* (Wiley Online Library, 2004).
- [2] I. Kominis, T. Kornack, J. Allred, and M. Romalis, *Nature* **422**, 596 (2003).
- [3] D. Budker and M. Romalis, *Nat. Phys.* **3**, 227 (2007), provided by the Smithsonian/NASA Astrophysics Data System.
- [4] J. R. Maze, P. L. Stanwix, J. S. Hodges, S. Hong, J. M. Taylor, P. Cappellaro, L. Jiang, A. Zibrov, A. Yacoby, R. Walsworth, and M. D. Lukin, *Nature* **455**, 644 (2008).
- [5] G. Balasubramanian, I. Y. Chan, R. Kolesov, M. Al-Hmoud, J. Tisler, C. Shin, C. Kim, A. Wojcik, P. R. Hemmer, A. Krueger, T. Hanke, A. Leitenstorfer, R. Bratschitsch, F. Jelezko, and J. Wrachtrup, *Nature* **455**, 648 (2008).
- [6] T. Wolf, P. Neumann, K. Nakamura, H. Sumiya, T. Ohshima, J. Isoya, and J. Wrachtrup, *Physical Review X* **5**, 041001 (2015).
- [7] M. S. Keshner, *Proceedings of the IEEE* **70**, 212 (1982).
- [8] J. Wikswo, J. Barach, and J. Freeman, *Science* **208**, 53 (1980).
- [9] J. Barry, M. Turner, J. Schloss, D. Glenn, Y. Song, M. Lukin, H. Park, and R. Walsworth, *ArXiv:1602.01056* (2016).
- [10] K. Jensen, R. Budvytyte, R. A. Thomas, T. Wang, A. Fuchs, M. V. Balabas, G. Vasilakis, L. Mosgaard, T. Heimburg, S.-P. Olesen, and E. S. Polzik, *ArXiv:1601.03273* (2016).
- [11] Y. Wang, J. Kirtley, F. Katmis, P. Jarillo-Herrero, J. Moodera, and K. Moler, *Science* **349**, 948 (2015).
- [12] B. Dellabatta, T. L. Hughes, M. J. Gilbert, and B. L. Lev, *Physical Review B* **85**, 205442 (2012).
- [13] A. Ajoy and P. Cappellaro, *Phys. Rev. A* **86**, 062104 (2012).
- [14] J. Cai, F. Jelezko, and M. B. Plenio, *Nature communications* **5** (2014).
- [15] F. Dolde, H. Fedder, M. W. Doherty, T. Nobauer, F. Remp, G. Balasubramanian, T. Wolf, F. Reinhard, L. C. L. Hollenberg, F. Jelezko, and J. Wrachtrup, *Nat. Phys.* **7**, 459 (2011).
- [16] N. F. Ramsey, *Molecular Beams* (Oxford University Press, 1990).
- [17] J. Van Wyk, E. Reynhardt, G. High, and I. Kiflawi, *Journal of Physics D: Applied Physics* **30**, 1790 (1997).
- [18] J. H. Scofield, *American Journal of Physics* **62**, 129 (1994).
- [19] W. Hill and P. Horowitz, *The art of electronics* (Cambridge University Press, 2015).
- [20] M. J. Biercuk, A. C. Doherty, and H. Uys, *J. of Phys. B* **44**, 154002 (2011).
- [21] A. Ajoy, G. A. Álvarez, and D. Suter, *Phys. Rev. A* **83**, 032303 (2011).
- [22] S. Kotler, N. Akerman, Y. Glickman, A. Keselman, and R. Ozeri, *Nature* **473**, 61 (2011).
- [23] K. Khodjasteh and D. A. Lidar, *Phys. Rev. Lett.* **95**, 180501 (2005).
- [24] B. J. Shields, Q. P. Unterreithmeier, N. P. de Leon, H. Park, and M. D. Lukin, *Phys. Rev. Lett.* **114**, 136402 (2015).
- [25] H. J. Mamin, M. Kim, M. H. Sherwood, C. T. Rettner, K. Ohno, D. D. Awschalom, and D. Rugar, *Science* **339**, 557 (2013).
- [26] T. Staudacher, F. Shi, S. Pezzagna, J. Meijer, J. Du, C. A. Meriles, F. Reinhard, and J. Wrachtrup, *Science* **339**, 561 (2013).
- [27] A. Ajoy, U. Bissbort, M. D. Lukin, R. L. Walsworth, and P. Cappellaro, *Phys. Rev. X* **5**, 011001 (2015).
- [28] L. Childress, M. V. Gurudev Dutt, J. M. Taylor, A. S. Zibrov, F. Jelezko, J. Wrachtrup, P. R. Hemmer, and M. D. Lukin, *Science* **314**, 281 (2006).
- [29] J. H. Shim, I. Niemeyer, J. Zhang, and D. Suter, *Phys. Rev. A* **87**, 012301 (2013).
- [30] A. Ajoy, Y. Liu, K. Saha, L. Marseglia, J.-C. Jaskula, U. Bissbort, and P. Cappellaro, *ArXiv:1604.01677* (2016).
- [31] See supplementary online material.
- [32] J. T. Hill, A. H. Safavi-Naeini, J. Chan, and O. Painter, *Nature communications* **3**, 1196 (2012).
- [33] T. Palomaki, J. Harlow, J. Teufel, R. Simmonds, and K. Lehnert, *Nature* **495**, 210 (2013).
- [34] S. Sridaran and S. A. Bhawe, in *Micro Electro Mechanical Systems (MEMS), 2012 IEEE 25th International Conference on* (IEEE,

- 2012) pp. 664–667.
- [35] H. Y. Carr and E. M. Purcell, *Phys. Rev.* **94**, 630 (1954).
- [36] S. Meiboom and D. Gill, *Rev. Sc. Instr.* **29**, 688 (1958).
- [37] T. Gullion, D. B. Baker, and M. S. Conradi, *J. Mag. Res.* **89**, 479 (1990).
- [38] S. Kolkowitz, Q. P. Unterreithmeier, S. D. Bennett, and M. D. Lukin, *Phys. Rev. Lett.* **109**, 137601 (2012).
- [39] T. H. Taminiiau, J. J. T. Wagenaar, T. van der Sar, F. Jelezko, V. V. Dobrovitski, and R. Hanson, *Phys. Rev. Lett.* **109**, 137602 (2012).
- [40] A. Abragam and B. Bleaney, *Electron Paramagnetic Resonance of Transition Ions* (Clarendon Press, Oxford, 1970).
- [41] M. Chen, M. Hirose, and P. Cappellaro, *Phys. Rev. B* **92**, 020101 (2015).
- [42] S. Sangtawesin and J. R. Petta, “Hyperfine-enhanced gyromagnetic ratio of a nuclear spin in diamond,” (2015), arXiv:1503.07464.
- [43] J. M. Taylor, P. Cappellaro, L. Childress, L. Jiang, D. Budker, P. R. Hemmer, A. Yacoby, R. Walsworth, and M. D. Lukin, *Nat. Phys.* **4**, 810 (2008).
- [44] W. M. Itano, J. C. Bergquist, J. J. Bollinger, J. M. Gilligan, D. J. Heinzen, F. L. Moore, M. G. Raizen, and D. J. Wineland, *Phys. Rev. A* **47**, 3554 (1993).
- [45] $t_d = 1.3\mu\text{s}$ in our experiments, although it could be as low as $\approx 350\text{ns}$.
- [46] T. Kornack, S. Smullin, S.-K. Lee, and M. Romalis, *Applied physics letters* **90**, 223501 (2007).
- [47] J.-C. Jaskula, K. Saha, A. Ajoy, and P. Cappellaro, in *APS Division of Atomic, Molecular and Optical Physics Meeting Abstracts* (2015).
- [48] G. A. Álvarez and D. Suter, *Phys. Rev. Lett.* **107**, 230501 (2011).
- [49] E. M. Kessler, I. Lovchinsky, A. O. Sushkov, and M. D. Lukin, *Phys. Rev. Lett.* **112**, 150802 (2014).
- [50] G. Arrad, Y. Vinkler, D. Aharonov, and A. Retzker, *Phys. Rev. Lett.* **112**, 150801 (2014).
- [51] W. Dür, M. Skotiniotis, F. Fröwis, and B. Kraus, *Phys. Rev. Lett.* **112**, 080801 (2014).
- [52] D. Vion, P. Orfila, P. Joyez, D. Esteve, and M. Devoret, *Journal of Applied Physics* **77**, 2519 (1995).
- [53] E. Bauch, J. Lee, S. Singh, M. L. Pham, K. Arai, and R. Walsworth, in *APS Division of Atomic, Molecular and Optical Physics Meeting Abstracts*, Vol. 1 (2015) p. 1155.
- [54] M. A. Nielsen, *Physics Letters A* **303**, 249 (2002).
- [55] M. Hirose and P. Cappellaro, Arxiv:1510.06801 (2015).
- [56] G. D. Fuchs, V. V. Dobrovitski, D. M. Toyli, F. J. Heremans, and D. D. Awschalom, *Science* **326**, 1520 (2009).
- [57] J. Scheuer, X. Kong, R. S. Said, J. Chen, A. Kurz, L. Marseglia, J. Du, P. R. Hemmer, S. Montangero, T. Calarco, B. Naydenov, and F. Jelezko, *New J. Phys.* **16**, 093022 (2014).
- [58] G. A. Álvarez, A. Ajoy, X. Peng, and D. Suter, *Phys. Rev. A* **82**, 042306 (2010).
- [59] A. M. Souza, G. A. Álvarez, and D. Suter, *Physical Review Letters* **106**, 240501 (2011).
- [60] L. M. Pham, D. Le Sage, P. L. Stanwix, T. K. Yeung, D. Glenn, A. Trifonov, P. Cappellaro, P. R. Hemmer, M. D. Lukin, H. Park, A. Yacoby, and R. L. Walsworth, *New J. Phys.* **13**, 045021 (2011).
- [61] M. Geiselmann, M. L. Juan, J. Renger, J. M. Say, L. J. Brown, F. J. G. de Abajo, F. Koppens, and R. Quidant, *Nat. Nanotech.* **8**, 175 (2013).
- [62] J. Baker-Jarvis and S. Kim, *Journal of research of the National Institute of Standards and Technology* **117**, 1 (2012).
- [63] F. Yan, S. Gustavsson, A. Kamal, J. Birenbaum, A. Sears, D. Hover, T. Gudmundsen, J. Yoder, T. Orlando, J. Clarke, *et al.*, arXiv preprint arXiv:1508.06299 (2015).
- [64] I. P. Prikhodko, S. A. Zotov, A. A. Trusov, and A. M. Shkel, *Microelectromechanical Systems, Journal of* **22**, 1257 (2013).
- [65] J. R. Schrieffer and P. A. Wolff, *Phys. Rev.* **149**, 491 (1966).
- [66] S. Bravyi, D. P. DiVincenzo, and D. Loss, *Annals of Physics* **326**, 2793 (2011).
- [67] W. Magnus, *Communications on Pure and Applied Mathematics* **7**, 649 (1954).
- [68] A. Ajoy and P. Cappellaro, *Phys. Rev. Lett.* **110**, 220503 (2013).
- [69] L. Cywinski, R. M. Lutchyn, C. P. Nave, and S. DasSarma, *Phys. Rev. B* **77**, 174509 (2008).
- [70] H. L. Flanagan and D. J. Singel, *J. Chem. Phys.* **87**, 5606 (1987).
- [71] V. Weis, K. Mobius, and T. Prisner, *Journal of Magnetic Resonance* **131**, 17 (1998).
- [72] V. Jacques, P. Neumann, J. Beck, M. Markham, D. Twitchen, J. Meijer, F. Kaiser, G. Balasubramanian, F. Jelezko, and J. Wrachtrup, *Phys. Rev. Lett.* **102**, 057403 (2009).
- [73] P. London, J. Scheuer, J.-M. Cai, I. Schwarz, A. Retzker, M. B. Plenio, M. Katagiri, T. Teraji, S. Koizumi, J. Isoya, R. Fischer, L. P. McGuinness, B. Naydenov, and F. Jelezko, *Phys. Rev. Lett.* **111**, 067601 (2013).
- [74] C. Belthangady, N. Bar-Gill, L. M. Pham, K. Arai, D. Le Sage, P. Cappellaro, and R. L. Walsworth, *Phys. Rev. Lett.* **110**, 157601 (2013).
- [75] S. R. Hartman and E. L. Hahn, *Phys. Rev.* **128**, 2042 (1962).
- [76] A. Pines, M. G. Gibby, and J. S. Waugh, *J. Chem. Phys.* **59**, 569 (1973).
- [77] H. Fedder, F. Dolde, F. Rempp, T. Wolf, P. Hemmer, F. Jelezko, and J. Wrachtrup, *Applied Physics B: Lasers and Optics* **102**, 497 (2011).
- [78] J.-P. Tetienne, L. Rondin, P. Spinicelli, M. Chipaux, T. Debuisschert, J.-F. Roch, and V. Jacques, *New J. Phys.* **14**, 103033 (2012).
- [79] T. Van der Sar, F. Casola, R. Walsworth, and A. Yacoby, *Nature Communications* (2015).
- [80] A. Wickenbrock, H. Zheng, L. Bougas, N. Leefer, S. Afach, A. Jarmola, V. M. Acosta, and D. Budker, *Appl. Phys. Lett.* **109**, 053505 (2016).

Supplementary Information: DC Magnetometry at the T_2 Limit

A. Ajoy, Y. X. Liu and P. Cappellaro

Research Laboratory of Electronics and Department of Nuclear Science & Engineering, Massachusetts Institute of Technology, Cambridge, MA

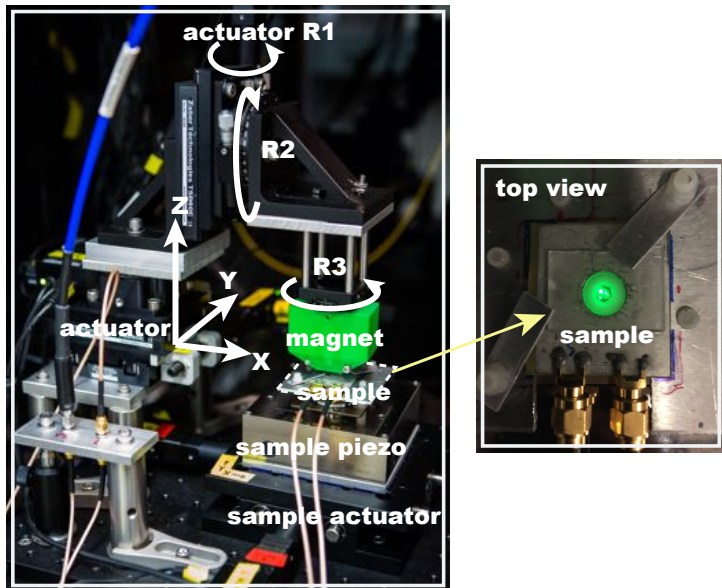


Figure S1. **Magnet setup.** Figure illustrates the magnetic field alignment setup used in our experiments. There are four motorized actuators for linear translation of the magnet in the X, Y and Z directions, along with a rotation stage R1. R2 and R3 are two unmotorized rotation stages. The magnet is a composite assembly of 12 magnets contained in the plastic green holder. By suitable alignment protocols, the magnetic field can be aligned to better than the Earth's field at the GSLAC.

SUMMARY

In this supplementary information, we provide detailed information about the experimental setup and the setup for magnetic field alignment. Also discussed are methods sampling the signal peak using quantum interpolation, and procedures used in fitting the experimental data.

I. EXPERIMENTAL SETUP

Our experimental sample consists of isotopically pure diamond (99.99% C-12, E6) containing NV centers produced via implantation and subsequent annealing. We used a home-built confocal microscope to address single NV centers. The details of the optical setup is identical to the one in [S1]. A 2mW 532 nm laser (SPROUT from Lighthouse Photonics) beam is first sent through an acousto-optic modulator (AOM, Isomet Corporation, M113-aQ80L-H) for switching and then focused using an oil immersion objective (Thorlabs N100X- PFO Nikon Plan Flour 1.3NA). The sample is mounted on a 3D-piezo scanner (NPoint) to scan the diamond for NV centers. The fluorescence excitation light is collected by the same objective, collimated, filtered from the 532 nm beam using a dichroic (Chroma NC338988) and then focused onto a pinhole for spatial filtering, and collected using a single-photon counting module (Perkin Elmer SPCM-AQRH-14).

We generate microwave pulses for XY8 sequences by direct synthesis of the pulses using 1.25 GS/s four channel arbitrary waveform generator [S2] (Model WX1284C, Tabor Electronics Ltd.) with tim-

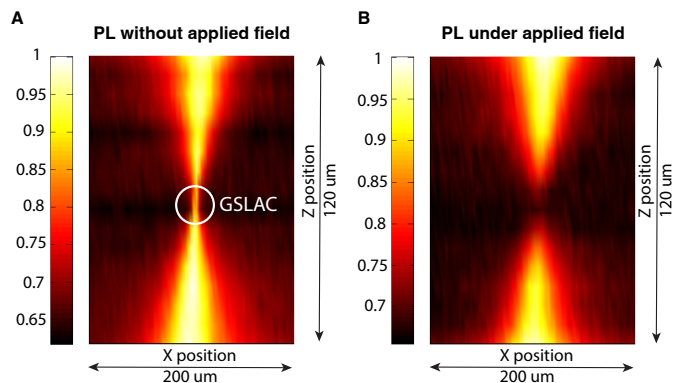


Figure S2. **Photoluminescence quenching under applied transverse fields.** (A) On the left panel is the NV center photoluminescence (PL) obtained in an XZ magnet scan, where the thin neck region corresponds to the GSLAC (see Fig. 13 of the main paper). (B) Corresponding PL in the presence of an applied voltage of +3.6V that generates a transverse magnetic field. As is evident there is a quenching of the PL close to the GSLAC. This could form the basis for all optical vector magnetometry with a single NV center.

ing resolution of $\Delta\tau = 1$ ns. The MW pulses are subsequently amplified using a high power amplifier (Minicircuits LZY22+) and delivered to the NV center through a $25\mu\text{m}$ Cu wire (Alfa Aesar) terminated in a 50Ω load. The AWG, the AOM and the single-photon counting module were gated using TTL pulses produced by a 500 MHz PulseBlaster (SpinCore). The DC magnetic fields used in the evaluation of sensitivity are created through voltage source (Berkeley Nucleonics BNC 575) driven on the same wire and combined with a bias tee (Minicircuits Z3BT-2R15G+). The experiments are done in a pulsed manner with a pulse rate about 0.5Hz, which ensures we operate within the bandwidth of the bias tee, and importantly also allows a concurrent measurement of intrinsic misalignment in alternate cycles to monitor thermal magnet drift. The applied voltage V produces a proportional magnetic field used to characterize the magnetometer, $B_e = \gamma_v V$, where from the experiments in Fig. 5 of the main paper we extract the value of $\gamma_v = 0.0407 \pm 0.0006$ G/V. This value also is in good agreement with an independent measurement of $\gamma_v = 0.0470$ G/V from the measured NV center Rabi frequency at 91MHz, since a 0dBm RF drive produced a Rabi frequency of 10MHz. We ascribe the slight discrepancy to transmission loss of the wire at RF frequencies.

For the experiments to determine the low pass filter function to signal noise (Fig. 4 of the main paper), we drive a single tone of low frequency voltage from a Rigol 1000D Arbitrary function generator through the same wire, and experimentally map out the filter function. The signal normalization in Fig. 4 is carried out by concurrently measuring the magnetometer signal under the corresponding RMS DC voltage and zero voltage (measuring the intrinsic misalignment).

II. SETUP FOR FIELD ALIGNMENT AT GSLAC

Here we describe our magnetic field alignment setup used in our experiments (see Fig. S1). Our magnet is a composite assembly of 10 N52 cubic magnets of 9.53mm edge (K&J Magnetics B666-N52)

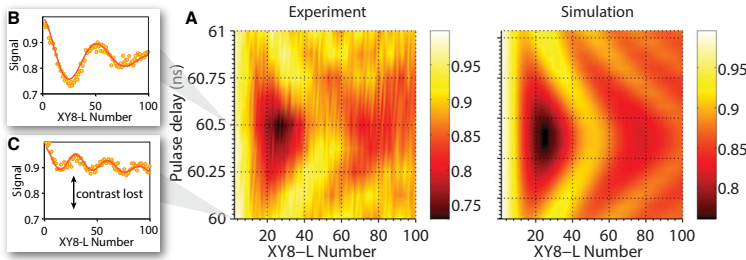


Figure S3. **Quantum interpolation to efficiently sample the signal peak.** (A) In a $\Delta\tau = 1\text{ns}$ window about the ^{14}N signal peak (Y axis), we sweep the XY8-L number (X axis), with $\Delta\tau$ being the timing resolution of our timing hardware (see also Fig. 2 of the main paper). These experiments are performed at $\Delta = 150\text{MHz}$. We use quantum interpolation effectively supersample 16 slices in this window. The signal obtained matches closely with the expected theoretical lineshape in Sec. II of the main paper (right panel), allowing us to estimate the static misaligned field in these experiments $|B_{\perp}| = 6.83\mu\text{T}$. (B-C) Lower inset demonstrates that without quantum interpolation there is significant loss of signal contrast, but the full contrast is recovered if one samples the signal peak (upper inset).

and 1.48T surface magnetization. The magnets are held together in a plastic case that was 3D printed. The magnet design was based on the construction used by the Ulm group [S3]. We define X to be the effective magnetization axis (N-S) of the magnet assembly, and is placed parallel to the edge of the [100] diamond. The magnet is mounted (Fig. S1) on a composite XYZ translation and rotation stage controlled by motorized actuators (Zaber TNA08A50 and Zaber RSW60A-T3 respectively). There are two more manual rotor stages for fine adjustment to ensure that the magnet surface is parallel to the sample edge. Magnet alignment close to the GSLAC is carried out primarily with the actuator based linear translation stages, details of which are presented in Appendix F of the main paper. The motorized rotation stage R1 (Fig. S1) allows a rapid transfer from the GSLAC to close to zero-field, and is used for debugging purposes.

NV center photoluminescence in a typical XZ magnet scan close to the GSLAC is shown in Fig. S2(A), where the narrow neck indicates the high sensitivity to field misalignment at the GSLAC. In the presence of a strong transverse field, applied through an external voltage, there is quenching of the photoluminescence, that can be exploited for all-optical vector magnetometry [S4].

III. QUANTUM INTERPOLATION TO EFFICIENTLY SAMPLE THE SIGNAL PEAK

In this section we describe the method of “quantum interpolation” that was employed in our experiments in order to precisely lock into the up-converted ^{14}N signal. The motivation for using quantum interpolation is that the delay between the π pulses in XY8 experiments has to be π/ω_0 , however this is often limited in precision in the finite timing resolution $\Delta\tau$ of the hardware used to generate the pulses (in our case $\Delta\tau = 1\text{ns}$). Indeed as the number of pulses N increases, there is a significant loss of contrast if one does not efficiently sample the true signal peak. The error goes as [S1], $\epsilon \approx \frac{1}{4}(N\alpha)^2\Delta\tau^2\left(2 - \frac{\alpha^2}{2}\right)^2$ that scales $\propto N^2(\Delta\tau)^2$, leading consequently to a severe loss of magnetometer sensitivity at large N .

We recently developed quantum interpolation [S1] as a means to overcome this hardware problem, allowing one to effectively *super-sample* the signal peak with arbitrarily high precision even with a

finite $\Delta\tau$. If the propagator $\mathcal{U}(\tau_k)$ describes action of a CPMG pulse sequence block, with π -pulses separated by a time $\tau_k = k\Delta\tau$, then quantum interpolation refers to the construction,

$$\mathcal{U}^N(\tau_{k+p/N}) = \mathcal{P} \left\{ \prod_{m=1}^{N-p} \mathcal{U}(\tau_k) \prod_{n=1}^p \mathcal{U}(\tau_{k+1}) \right\} \approx \mathcal{U}^N(\tau_{k+p/N}), \quad (\text{S1})$$

that allows the construction of supersamples $\tau_{k+p/N}$ that cannot usually be accessed. Here the permutation \mathcal{P} refers to an optimal sequence ordering that minimizes error in the construction, the error going as $\mathcal{O}(\Delta\tau^2)$. Importantly the number of additional timing samples achievable via quantum interpolation scales linearly with the total number of pulses [S1], allowing us to completely mitigate the problem of hardware finite hardware resolution for increasing N .

In Fig. 2 of the main paper quantum interpolation is used to sample the ^{14}N signal peak to about 48 times higher resolution (20.8ps) than set by our hardware, allowing us to determine the exact peak position at $\approx 60.45\text{ns}$. The signal lineshape can be described as a modified sinc-function with a slight asymmetry about the peak, and can be evidently discerned in Fig. 2 of the main paper. The power of the technique is demonstrated in Fig. S3, where we obtain the magnetometry signals similar to Fig. 2 of the main paper for 16 different supersamples in the $\Delta\tau$ window set by our hardware. There is significant signal loss if one does not sample the true ^{14}N signal peak Fig. S3(B-C). The figure also illustrates that the experimental data closely matches the theoretically expected sinusoidal lineshape. The obtained “chevron” patterns in Fig. S3(A) are exactly identical to those in two-spin exchange [S5]. Overall, this illustrates that the quantum interpolation construction is indeed of low error, and is critical to obtaining the true ^{14}N signal peak used in ancilla assisted DC magnetometry.

IV. DATA ANALYSIS

For clarity, we now detail the procedure for the fitting of experimental data that is used to calculate the corresponding error bars, primarily in Fig. 3, Fig. 4 and Fig. 5 of the main paper. We use a Monte-Carlo approach to estimate the uncertainty of the various fit parameters following Ref. [S1].

Let us denote the fit parameters for our model by \mathbf{P} . For a given set \mathbf{P} , our theoretical model provides a non-linear functional relation $y = f(x|\mathbf{P})$. Given a measured set of data points $\{x_n\}$ and $\{y_n\}$, we determine the optimal set of parameters \mathbf{P}_{opt} by minimizing $\chi^2 = \sum_n [y_n - f(x_n|\mathbf{P})]^2 / \sigma_y^2$. Here we have assumed that the statistical error σ_y of the measured data points is identical for all points.

Once \mathbf{P}_{opt} , the statistical uncertainty of y_m is estimated from the deviation from the optimally fitted function $\sigma_y^2 \approx \sum_n [y_n - f(x_n|\mathbf{P}_{\text{opt}})]^2 / (N-1)$, where N is the number of data points. The value of σ_y obtained by this procedure yields sets a lower bound for the true statistical uncertainty, as any systematic deviation of the fitted function (i.e. if we have not captured the underlying true functional form in our theoretical model) increases σ_y . Subsequently the uncertainty in the fit parameters \mathbf{P} can be estimated beyond linear order by generating artificial data sets of points $\{x_n\}$ and $\{y_n\}$ statistically distributed around $f(x_n|\mathbf{P}_{\text{opt}})$, subsequently performing a fit for each data set. We assume a Gaussian distribution for the generation of these data points, an assumption which can be verified by inspecting the distribution of $\delta y_n = y_n - f(x_n|\mathbf{P}_{\text{opt}})$ in the original data. Repeating this procedure yields a distribution of fit parameters of which the distributional form, confidence intervals and standard deviation for the individual parameters can be extracted.

-
- [S1] A. Ajoy, Y. Liu, K. Saha, L. Marseglia, J.-C. Jaskula, U. Bissbort, and P. Cappellaro, *ArXiv:1604.01677* (2016).
- [S2] [wx1284c Data Sheet](#).
- [S3] T. Unden, P. Balasubramanian, D. Louzon, Y. Vinkler, M. B. Plenio, M. Markham, D. Twitchen, A. Stacey, I. Lovchinsky, A. O. Sushkov, M. D. Lukin, A. Retzker, B. Naydenov, L. P. McGuinness, and F. Jelezko, *Phys. Rev. Lett.* **116**, 230502 (2016).
- [S4] A. Wickenbrock, H. Zheng, L. Bougas, N. Leefer, S. Afach, A. Jarmola, V. M. Acosta, and D. Budker, *Appl. Phys. Lett.* **109**, 053505 (2016).
- [S5] A. Ajoy and P. Cappellaro, *Phys. Rev. A* **85**, 042305 (2012).